Towards Optimal Collimator Design for the PEDRO Hybrid Imaging System

Chuong V. Nguyen, John E. Gillam, Jeremy M. C. Brown, David V. Martin, Dmitri A. Nikulin, and Matthew R. Dimmock

***Abstract*—The Pixelated Emission Detector for RadiOisotopes (PEDRO) is a hybrid imaging system designed for the measurement of single photon emission from small animal models. The proof-of-principle device consists of a Compton-camera situated behind a mechanical collimator and is intended to provide optimal detection characteristics over a broad spectral range, from 30 to 511 keV. An automated routine has been developed for the optimization of large-area slits in the outer regions of a collimator which has a central region allocated for pinholes. The optimization was tested with a GEANT4 model of the experimental prototype. The data were blurred with the expected position and energy resolution parameters and a Bayesian interaction ordering algorithm was applied. Images were reconstructed using cone back-projection. The results show that the optimization technique allows the large-area slits to both sample fully and extend the primary field of view (FoV) determined by the pinholes. The slits were found to provide truncation of the back-projected cones of response and also an increase in the success rate of the interaction ordering algorithm. These factors resulted in an increase in the contrast and signal-to-noise ratio of the reconstructed image estimates. Of the two configurations tested, the cylindrical geometry outperformed the square geometry, primarily because of a decrease in artifacts. This was due to isotropic modulation of the cone surfaces, that can be achieved with a circular shape. Also, the cylindrical geometry provided increased sampling of the FoV due to more optimal positioning of the slits. The use of the cylindrical collimator and application of the transmission function in the reconstruction was found to improve the resolution of the system by a factor of 20, as compared to the uncollimated Compton camera. Although this system is designed for small animal imaging, the technique can be applied to any application of single photon imaging.**

***Index Terms*—Compton scattering enhancement, multiple pinhole, PEDRO.**

I. INTRODUCTION

SINGLE photon emission imaging devices are typically based on either mechanical [1]–[3] or electronic (Compton) [4] collimation. Mechanical collimators are composed of high Z materials that modulate the photon flux incident on the detector. This allows a high resolution estimate of the radio-tracer distribution to be obtained at the expense of system sensitivity.

Manuscript received November 15, 2010; revised March 04, 2011; accepted March 21, 2011. Date of publication May 05, 2011; date of current version June 15, 2011. This work was supported by the Cooperative Research Center for Biomedical Imaging Development Ltd (CRC-BID), established and supported under the Australian Government's Cooperative Research Centers Program.

C. V. Nguyen and M. R. Dimmock are with the School of Physics, Monash University, Melbourne, VIC 3800, Australia and also with the Monash Node of the CRC for Biomedical Imaging Development, Melbourne, VIC 3800, Australia (e-mail: chuong.nguyen@monash.edu; matthew.dimmock@monash.edu).

J. E. Gillam is with the Instituto de Fisica Corpuscular (IFIC), Universidad de Valencia-CSIC, Valencia, Spain.

J. M. C. Brown and D. V. Martin are with the School of Physics, Monash University, Melbourne, VIC 3800, Australia.

D. A. Nikulin is with the Monash Node of the CRC for Biomedical Imaging Development, Melbourne, VIC 3800, Australia.

Color versions of one or more of the figures in this paper are available online at http://ieeexplore.ieee.org.

Digital Object Identifier 10.1109/TNS.2011.2134869

Electronic collimation requires no physical modulation of the incident flux. However, the resolution of the image estimate is limited by the detector position and energy resolutions and Doppler broadening. Typically, highly pixelated semiconductor detectors are utilized as they provide superior energy resolution over conventional scintillation detectors. Following a Compton scattered event an additional tracking or interaction ordering step is performed to determine the first and second interactions that define the cone of response (CoR). The subsequent back-projection of CoRs from many such events yields a high sensitivity, but generally low resolution, estimate of the radioisotope distribution.

The Pixelated Emission Detector for RadiOisotopes (PEDRO) [5] is a proof of principle hybrid imaging system being developed to investigate the combination of mechanical and electronic (hybrid) collimation [6]–[9]. The intended energy range for operation is from 30 to 511 keV. The optimization of this hybrid system should yield image estimates with both high resolution and high sensitivity. This will be achieved through reconstruction of both lines of response (LoRs) from well-defined pinholes in the center of the collimator and modulated CoRs from large-area apertures in the outer-regions. The aim of such an optimization is to increase the number of photons which impinge on the detector stack without polluting the pinhole projection data. It is expected that the modulated CoRs should complement the pinhole data, extending the field of view (FoV) and improve the iterative reconstructions. In order to achieve this goal, several constraints must be considered in the design of the large-area slits:

- The apertures must be able to focus the incident photons at pre-determined regions of the detector stack.
- The photons should be directed in a manner which maximizes the probability of a Compton scatter being the primary interaction mechanism.
- The overlap between the pinhole FoV and the large-area slit FoV should be maximized in order that the resulting images can be combined and/or quantitatively compared.

This paper focuses on collimator optimization for photons with an incident energy $e_0 = 140$ keV. The experimental prototype that is currently being tested is introduced in Section II. The 2D-optimization of slit geometries and the extension to 3D are described in Section III. This section also details the optimization procedure and the Compton reconstruction algorithm. Quantified results from Monte-Carlo simulations of the experimental prototype are presented in Sections IV and V. Finally, the results and directions for future work are provided in Section VI.

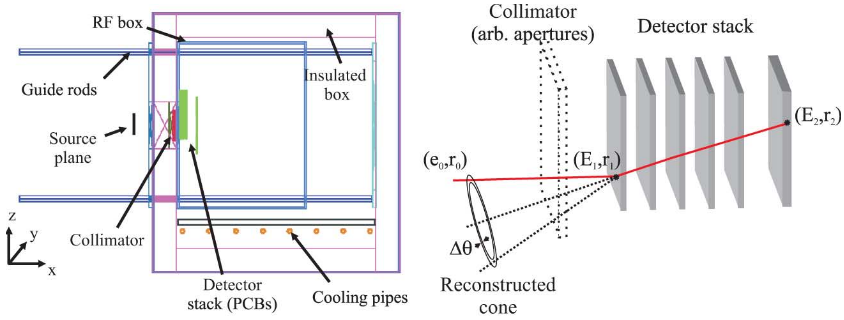

Fig. 1. (a) A schematic representation of the PEDRO experimental prototype. (b) A schematic illustration of the collimated Compton camera with an incoherent scatter with energy deposits E_1 and E_2 at two interaction locations r_1 and r_2. The left-most layer is the collimator shown with dashed lines to represent any arbitrary aperture configuration. The next 5 layers are Si detectors. The final layer is a CdTe detector.

II. Experimental PEDRO

The experimental prototype (shown schematically in Fig. 1(a) being developed consists of an interchangeable aperture array positioned in front of a Compton camera. The Compton camera is composed of a stack of Silicon double-sided strip-detectors (Si-DSSDs) and a Cadmium Telluride (CdTe) hybrid-pixel detector (HPD). The aperture array has been designed to accommodate pinholes, slits and open-areas as the optimal configuration is as yet undetermined. Ideally, to maximise the detection efficiency of the PEDRO, many detector layers would be incorporated. However, due to the limit imposed by the budget for the project, only 5 Si-DSSDs and 1 HPD are used in the system.

Each of the 5 Si-DSSDs that comprises the stack was fabricated by Centro Nacional de Microelectronica. The active volume of each is $0.8 \times 31.9 \times 31.9\ \mathrm{mm}^3$, which is segmented into 64 orthogonal strips on each side. The strips each have a width of $400\ \mu\mathrm{m}$ and gap of $100\ \mu\mathrm{m}$. The detectors are bonded to GM-IDEAS VA64TA Application Specific Integrated Circuits (ASICs) and are operated in a DC coupled configuration.

The HPD [10] is currently being developed at the Monash Centre for Synchrotron Science (MCSS), as part of a project being conducted by MCSS as a participant of the Cooperative Research Centre for Biomedical Imaging Development (CRCBID). It consists of a $51.2 \times 51.2 \times 2.0\ \mathrm{mm}^3$ CdTe crystal with a 256×256 pixelated anode. The crystal will be bump-bonded to the 0.2 mm pitch custom-designed ASIC.

The full-width-half-maximum (FWHM) of the detector energy resolution is dependent on the detector material, applied bias and incident energy. The FWHM is of the form $y = ax + b$, where x is the deposited energy in keV, and a and b are material-dependent parameters. In this work, the values of a and b are chosen to be 0.01 and 2.0 for Si detectors, and 0.015 and 4.0 for CdTe detector. These values were approximated from the distributions expected from the experimental prototype detectors.

The multiplexed outputs from both the VA64TA1 and HPD ASICs will be read out and controlled through the Generic Data AcQuisition (GDAQ) system [11], also developed at MCSS. Software (DAX) has been developed in-house to enable precise control and readout functionality for synchronized coincidence data collection.

III. Collimator Design Optimization

The predominant interaction mechanism through which gamma rays interact in the detectors varies significantly with the source energy and detector material. For incident photons where $e_o \leq 50\ \mathrm{keV}$ photoelectric absorption occurs primarily in the Si-DSSDs, minimizing the flux incident on the HPD. For $50 < e_0 \leq 100\ \mathrm{keV}$, photons that interact in the Si-DSSDs will undergo either incoherent (Compton) scattering or photoelectric absorption, while those that interact in the CdTe will be predominantly photoelectrically absorbed. Therefore, the experimental configuration is optimal when operated as a multi-resolution Single Photon Emission Imaging (SPEI) device. For this mode of operation, small apertures (pinholes) are required to reconstruct a high-resolution estimate of the source by back-projection of LoRs into the imaging volume. The resolution of the reconstructed image depends on the size of the pinhole(s) and detector pixels, assuming full energy deposition. To increase the sensitivity of the system, many pinholes may be utilized. This typically results in the degree of multiplexing of the projection data increasing with distance from the collimator.

For incident photons with energies $100\ e_0 \leq 700\ \mathrm{keV}$, the probability of incoherent (Compton) scattering becomes dominant in the Si-DSSDs and the data consists of events where the primary interaction is either photo-electric absorption or Compton scattering. For the latter, Compton data can be used to help restrict the number of pinholes through which the incident photon may have passed via de-multiplexing [12]. As well as increasing the number or density of pinholes, the sensitivity can also be increased by the introduction of large-area apertures. This is only feasible if the primary interaction mechanism for photons that pass through these apertures is Compton scattering. The resulting CoRs measured are modulated by the aperture, limiting the range of possible incident photon trajectories and making each cone surface more informative. If a photon passes through a large-area aperture and a single interaction is recorded (due to the process of photoelectric absorption or the gamma ray scattering out of the stack), only an LoR can be back-projected. The axis of the line is defined between the center of the pixel and the aperture. The uncertainty of the line will be dominated by the size of the aperture and will be significantly more blurred than an equivalent LoR back-projected through a well-defined pinhole. The LoRs from pinholes give rise to high-resolution, low-sensitivity measurements while the large-area aperture CoRs yield higher-sensitivity, lower-resolution measurements in comparison. It should be noted that the addition of large-area apertures within the collimator needs careful consideration so that the high resolution pinhole data is not contaminated, but instead enhanced when combined with the CoRs.

For photons where $e_0 \geq 700$ keV, the photoelectric absorption cross-section is insignificant compared to that for Compton scattering and the optimization of the collimator becomes ambiguous. At these energies, it is likely that the inclusion of a collimator would degrade the image estimate as the edges of the apertures become transparent to the gamma rays and the collimator serves only as a scattering target.

Calculation of each aperture geometry is governed by many experimental factors, including e_0 and the material properties such as the mass-attenuation coefficient and K-edge location. The system will be operated over a broad energy range, so it is not practical to utilize a single geometry over this range as the level of scatter and penetration into the collimator increases with energy. To address this issue, an interchangeable aperture mounting structure has been constructed which is able to support a maximum thickness of 1.50 cm of Tungsten inserts, sufficient to limit the transmission at 511 keV to $< 3\% (3\sigma)$. Up to nine aperture arrays, consisting of pinholes, slats or open spaces, can be mounted as inserts in the volume. The work presented here assumes that the central region of the collimator is reserved for an arbitrary number of pinholes for forming a high resolution image. The optimization then determines the number, shape and position of large-area slits to be added to the outer collimator regions that maximize the system sensitivity or FoV. As stated previously, the quality of the image estimate generated from the detector data depends on the interaction sequence of each event. For the optimization of large-area slits, the most informative data can be obtained from photons that Compton scatter where both the primary and secondary interaction sites can be resolved. Events for which any of the first two interactions are not recorded and or resolved will decrease the signal-to-noise ratio (SNR) in the image estimate, unless appropriately weighted. This is because the back-projection axis from an unresolved Compton event would be oriented in the wrong direction, while the back-projected LoR from a photoelectric-absorption event would have a large uncertainty determined by the open-area of the slit. The two event categories described above will be referred to as resolved and unresolved measurements.

Optimisation parameters can include the FoV, sensitivity and ultimately the overall image quality. For the investigations presented herein, the openings of the slits were adjusted so that the following criteria were met:

- The FoV of the slit-set was constrained to at least fully sample the extents of the FoV of the pinholes. This criterion was selected in order that in future investigations, the difference in imaging performance between the slits and pinholes may be assessed.
- Provided criterion one held, the sensitivity of the detector array was maximized.

For the 3D realization of the collimator, the resultant image quality was also quantified.

A. Two-Dimensional Collimator Design

The first step towards developing an optimization routine was to generate a 2D ray-tracing version of the model illustrated in Fig. 2(a). This was utilized to investigate the 2D geometric constraints of the experimental PEDRO configuration. The optimization then followed a multi-step procedure:

1) *Geometric configuration*. The geometries and locations of the source, detector stack and collimator are fixed. The values that were chosen to describe the experimental prototype are presented in Table I. For this investigation, the three pinholes were positioned at the corners of an equilateral triangle with side-length of 6.0 mm. In 2D, the pinhole dimensions were calculated from the projection onto the *y*-axis. This configuration then allowed the source projections to be determined. It should be noted that in all of the following discussion, the pinholes were used as place-holders. However, they were not made transparent to the incident photons. The source was a uniform circular distribution on the *y*-*z* plane. In 2D, this distribution was a projection onto the *y*-axis. The *y*-*z* dimensions of the HPD were fixed to be the same as the size of the pinhole-source projection at the *x*-location of the detector. To maintain the directionality of the collimator, a minimum thickness of Tungsten (L_W) through which any ray-traced photon trajectory must pass is defined by the user. For this investigation, L_W was fixed at 1.02 mm for which 95% (or 2σ) of 140 keV incident photons are stopped in the collimator.
2) *Upper limit of FoV*. A line from location **H** (Fig. 2(a)) at the top edge of the HPD is chosen to connect to the upper edge of the FoV (source). The line intersects the collimator walls at **A** and **B**. Locations **A** and **B** mark the limits of the upper and lower sides of the slit through which gamma rays can pass without impinging on the HPD. This location is chosen as photons that pass through the large-area slits and are incident on the HPD are likely to undergo photo-electric absorption. Such photons result in an unresolved event-type and contaminate the pinhole projection. Locations **C** and **D** lying on the vector **AB** are then selected at a distance from **A** and **B** equal to L_W as **AC** and **BD** become the edges of the slit.
3) *Lower limit of FoV*. Location **G** is the position of the top edge of the first Si-DSSD. Two vectors are then defined that connect **G** to **C** and **D** and intersect with the collimator walls at **E** and **F**. The geometry of the slit is now defined by locations **A**, **B**, **C**, **D**, **E** and **F**. This slit is the primary large-area aperture that maximizes the ratio of resolved to unresolved event types without polluting the pinhole projection data. The FoV of the aperture is defined by the vectors **HA** and **GE**.
4) *Utilization of remaining space*.More slits can be added to the remaining section of the collimator by starting new lines from location **H**. The addition of subsequent slits must not violate the condition that the minimum thickness of any ray-traced from the source and crossing the HPD is greater than L_W.
5) *Refinement of slit locations*. The locations of **A** or **B** of the slits can be adjusted for the desired final FoV of the source. Currently the locations are chosen by considering the slit-to-slit and slit-to-pinhole distances and selecting the set that produces the greatest transmission within the FoV of the source.

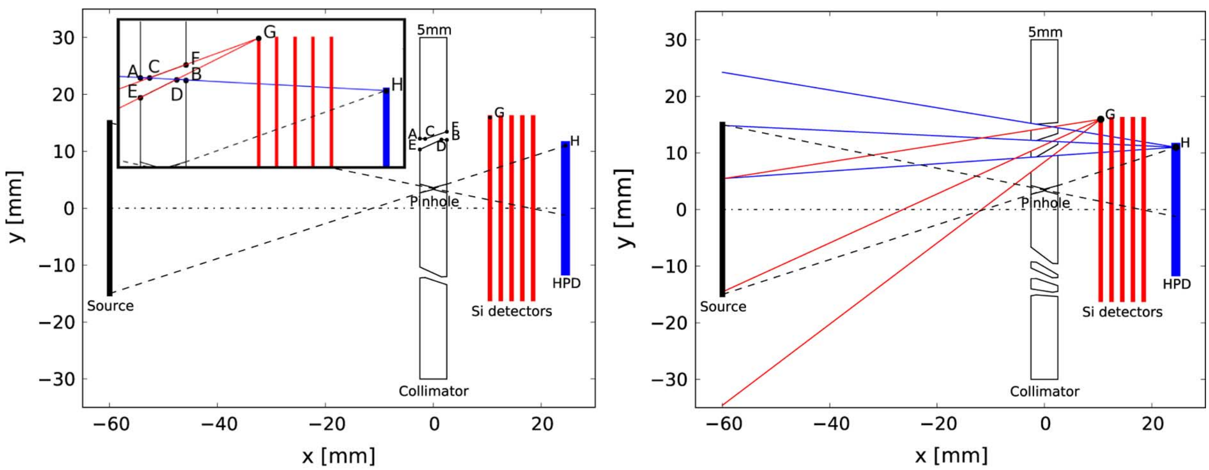

(a) (b)

Fig. 2. (a) A schematic representation of the 2D ray-tracing collimator optimization. This was performed for a single large-area slit with 3 pinholes in an equilateral triangle configuration around the collimator center. The geometry of the slit is now defined by locations A, B, C, D, E and F, determined from the optimisation. Inset is a zoomed view of the geometry of the slit and the ray tracing to form the slit. The limit-case lines connecting any point within the slit to G and H mark the regions of the detectors for which photons incident on the collimator can interact. Events for which the primary interaction of a Compton scatter sequence occurs in these regions are used for Compton back-projection. The oblique dashed lines show the projection of the source through one of the 3 pinholes on the collimator. The projections of the source through the 3 pinholes partially overlap in the centre region of the HPD. This is the reason why the lower end of the pinhole projection on the HPD goes below the centre line in this figure. (b) The extension of the optimization to show multiple large-area slits above and below the central region, pre-allocated for the pinholes.

TABLE I
THE GEOMETRIES OF EXPERIMENTAL COMPONENTS (SEE FIG. 2(a) AND (b))

	Size (y-z) [mm]	Pixel size (y-z) [mm]	Thickness (x) [mm]	Location (x) [mm]
Source	30.0 (dia.)	N/A	0.0	-60.0
Collimator	60.0 (dia.)	N/A	5.0	0.0
Si-DSSDs	31.9×31.9	0.2×0.2	0.8	9,11,13,15,17
HPD	20.7×20.7	0.5×0.5	2.0	23.0

Fig. 2(b) shows the extension of the design to a collimator with 3 slits on each of the upper and lower sides. The limiting cases of the ray tracing are shown on the upper part of the collimator. At each slit, two vectors that define the range of the FoV are defined between locations **G** and **H** and the upper and lower edges of the slit. The limit-case lines connecting any point within the slit to G and H mark the regions of the detectors for which photons incident on the collimator can interact. Events for which the primary interaction of a Compton scatter sequence occurs in these regions are used for Compton back-projection. The oblique dashed lines show the projection of the source through one of the 3 pinholes on the collimator. The projections of the source through the 3 pinholes partially overlap in the centre region of the HPD. This is the reason why the lower end of the pinhole projection on the HPD goes below the centre line in this figure.

The effective transmission ET_W as a function of emission location y and angle α (angle of photon emission from the source plane) of the optimized large-area slits, can be calculated from,

$$ET_W(y,\alpha) = \exp\left[-\mu_W^t L_W(y,\alpha)\right] \tag{1}$$

where $L_W(y,\alpha)$ is the total depth of Tungsten that the ray intersects with the collimator, and μ_W^t is the total linear attenuation coefficient for Tungsten at the source energy. For 140 keV photons, $\mu_W^t = 36.2\ \mathrm{cm}^{-1}$. In the following discussions, μ will always refer to the *linear* attenuation coefficient. The effective transmission outside the bounds of the collimator is neglected. The mean effective transmission (ET) from each emission location in y is given by,

$$\langle ET_W\rangle(y) = \frac{1}{\pi}\int_{-\pi/2}^{\pi/2} ET_W(y,\alpha)d\alpha. \tag{2}$$

After traversing the collimator, the modulated photon flux impinges on the Si-DSSD stack. The effective attenuation (EA) of the stack is given by,

$$EA_{Si}(y,\alpha) = 1 - \exp\left[-\mu_{Si}^t L_{Si}(y,\alpha)\right] \tag{3}$$

where $L_{Si}(y,\alpha)$ is the total depth of Si and μ_{Si}^t is the total linear attenuation coefficient of Si. For 140 keV, $\mu_{Si}^t = 0.35\ \mathrm{cm}^{-1}$. The effective sensitivity (ES) of the system is proportional to the product of the collimator transmission and the attenuation in the Si-DSSD stack, given by,

$$\langle ES_{sys}\rangle(y) = \frac{1}{\pi}\int_{-\pi/2}^{\pi/2} ET_W(y,\alpha)EA_{Si}(y,\alpha)d\alpha. \tag{4}$$

If the sampled emission angles are binned (discretized), (2) and (4) become,

$$\langle ET_W\rangle(y) = \frac{1}{\pi}\sum_{i=0}^{N} ET_W(y,\alpha_i)\Delta\alpha \tag{5}$$

$$\langle ES_{sys}\rangle(y) = \frac{1}{\pi}\sum_{i=0}^{N} ET_W(y,\alpha_i)EA_{Si}(y,\alpha_i)\Delta\alpha \tag{6}$$

where $\Delta\alpha = \pi/N$, N is the number of angular bins and $\alpha_i = -\pi/2 + i\Delta\alpha$.

Fig. 3(a) presents an example of rays emitted from a point at the center of the source distribution ($y = 0$). The limits of the ray vectors show the range in α of the trajectories utilized to calculate the effective transmission at this location. All the rays

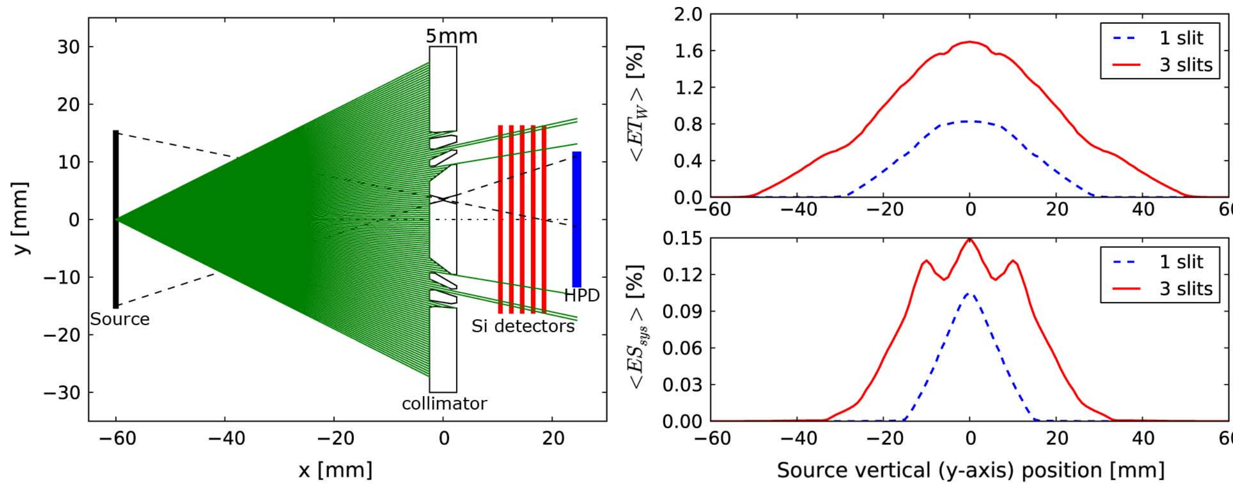

(a) (b)

Fig. 3. (a) Illustration of ray tracing for 500 photons emitted from location $y = 0$. All the rays with an effective transmission below 5% are visualized as being stopped in the collimator. (b) Line-plots of the calculated effective transmission (upper) and system effective sensitivity (lower). Solid and dashed lines represent the distributions for the collimators with one and three slits, respectively. Note that the y-range in (b) is larger than that in (a). The FoV of the system for both the one and three slit geometries extends beyond the range of the distributed source. The magnitude and range of the sensitivity function is significantly larger for three slits with respect to the one slit geometry.

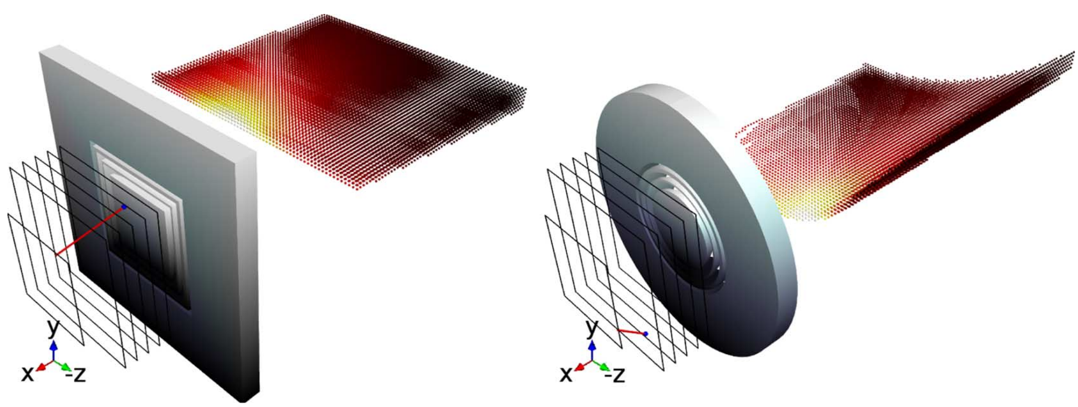

(a) (b)

Fig. 4. (a) A 3D representation of the triple slit square collimator configuration. (b) A 3D representation of the triple slit cylindrical collimator configuration. The dots in front of the collimator represent the image voxels where the transmission $p_t = 1$. The shades of the dots represent the values of CoR at the voxels. The transparent squares represent the detector layers. The short straight line shows the recoil photon trajectory connecting the first (shown as solid dot) and second interactions forming the CoR.

with ET_W below 5% are shown to be stopped in the collimator.

Fig. 3(b) shows the distributions of $\langle ET_W \rangle$ and $\langle ES_{sys} \rangle$ as the number of slits included is increased. The distribution was calculated in 1.0 mm increments along the y-axis. At each location, 5000 photons were uniformly emitted within an angular range of 2π. When there are no slits in the collimator, $\langle ET_W \rangle$ and $\langle ES_{sys} \rangle$ are negligible. When changing from one slit to three slits, $\langle ET_W \rangle$ and $\langle ES_{sys} \rangle$ are significantly increased as expected. The FoV is also significantly increased with the extension to three slits.

B. Three-Dimensional Collimator Model in GEANT4

The optimized collimator, described in the previous section, was extended to 3D and modelled in GEANT4 [13]. The simulations incorporated all of the experimental components: detectors; motherboards; housing; RF-shielding; the collimator and the source. In GEANT4, the collimator was constructed from two parts, an inner section reserved for pinholes and an outer part containing slits. The slits in the outer sections were formed using the G4BREPSolidPolyhedra class objects to avoid repeating solid subtractions that can cause errors in GEANT4 ray-tracing. This object class also made the extension from square to cylindrical configurations trivial as the input just required an increase in the number of sides of each polyhedron. Fig. 4(a) and (b) show the two 3D configurations modelled in GEANT4. The first collimator design was composed of three concentric square slits that were matched to the geometry of the Cartesian detector stack. The second was a cylindrical geometry, which better used the space surrounding the central pinhole region. In reality, the individual parts of the collimators need extra mechanical supports to be held together in place. A solution is to fill in slit spaces with a low density rigid plastic foam [15].

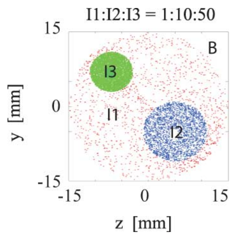

Fig. 5. The triple intensity planar phantom source distributions. The three circles (radius = 15.0, 6.0, and 4.0 mm) have relative intensities of 1:10:50. Region B is the background of the phantom with zero intensity. The source is on *y-z* plane.

To study the performance of both collimator configurations, simulations were performed with a distributed source of $e_0 = 140\ \mathrm{keV}$ shown in Fig. 5. The source distribution was a triple intensity planar phantom consisting of three circular distributions *I1*, *I2* and *I3*. The outer circle (*I1*) had a radius of 15.0 mm and the two inner circles had radii of 6.0 mm and 4.0 mm. The smallest radius of the circles was approximately 2 times the average gap of the slits, to account for the expected size of the point-spread-function (PSF). The three distributions had relative intensities of 1:10:50.

An additional study was performed to investigate the system PSF. A point-source which emitted 140 keV photons was positioned at the center of the FoV for geometries that included the Compton camera stack both with and without a physical collimator.

The reconstruction algorithm used for both the distributed and point source investigations is described in Section III-C.

C. Compton Reconstruction

Estimates of the source distributions were formed utilizing Compton-cone reconstruction with consideration of the transmission properties of the collimator. For an incident gamma ray emitted from location $\mathbf{r_0}$, with energy e_0, the Compton scatter angle θ_C at the first interaction is related to the energy deposited E_1 (see Fig. 1(b)) by,

$$\cos\theta_C = 1 + m_e c^2 \left(\frac{1}{e_0} - \frac{1}{e_1}\right) \tag{7}$$

where $e_1 = e_0 - E_1$ is the energy carried by the recoil photon after the interaction. For an ideal system, the scattering angle θ_C defines a CoR on which the photon emission location originated. For a finite imaging volume in a realistic system the intersection of the CoR with the imaging volume gives a probability distribution of the likelihood that the photon was emitted from each voxel in the volume. The probability density function Φ of the CoR can be generally expressed as:

$$\Phi(\mathbf{r_v}) = \frac{1}{4\pi} p_t(\mathbf{r_v}) \cdot p_{v1} \cdot p_C \cdot p(\mathbf{r_{v1}}, \wedge | \theta_C, E_1) \cdot p_{12} \cdot p_i \tag{8}$$

where $\mathbf{r_v}$ is the location of an arbitrary voxel inside the imaging volume, $\mathbf{r_{v1}}$ is the vector from $\mathbf{r_v}$ to the cone apex $\mathbf{r_1}$, $p_t(\mathbf{r_v})$ is the collimator transmission function, p_{v1} is the probability that the gamma ray from $\mathbf{r_v}$ reaches the interaction location $\mathbf{r_1}$ given it traverses the collimator, p_C is the probability that a Compton scatter occurs at $\mathbf{r_1}$, p_{12} is the probability that the photon reaches the second interaction location $\mathbf{r_2}$, p_i is the probability of an interaction at $\mathbf{r_2}$ and $p(\mathbf{r_{v1}}, \wedge | \theta_C, E_1)$ is the probability of the emission at $\mathbf{r_v}$ Compton scattering at an angle θ_C resulting in a measured energy E_1. $\wedge$ denotes cone surface. The last of these probabilities is the double differential cross section, which can be approximated by,

$$p(\mathbf{r_{v1}}, \wedge | \theta_C, E_1) = \frac{1}{2\pi r_{v1}^2} p_\wedge(\theta_v \mid \theta_C) \cdot p(\theta_C) \tag{9}$$

where θ_v is the angle between $\mathbf{r_{v1}}$ and the vector of the cone axis $\mathbf{r_{12}}$, $p(\theta_C)$ is the scattering function and $p_\wedge(\theta_v \mid \theta_C)$ is the CoR with angular uncertainty. The probability density function (PDF) of CoR can be approximated by [14],

$$p_\wedge(\theta_v \mid \theta_C) = \left[0.9 \exp\left(-\frac{(\theta_v - \theta_C)^2}{2\sigma^2}\right) + 0.1 \exp\left(-\frac{(\theta_v - \theta_C)^2}{2(3\sigma)^2}\right)\right] \tag{10}$$

where σ is chosen to be $\Delta\theta/2.35$. It should be noted that (10) is an approximation, both in the shape and the width of the function. This approximation is reasonable as long as Doppler broadening is the dominant factor in $\Delta\theta$.

In this study, image reconstruction is performed by CoR back-projection. In order to preserve the intensity, the sum of the contributions of all voxels for each CoR was normalized to 1.0. This implies that the source is contained by the image volume. Additional detailed description of the implementation of the Compton back-projection can be found in the Appendix.

IV. Contrast and Signal-to-Noise Results

A. GEANT4 Simulation Results

The simulations were performed on the Nimrod/G computing cluster at Monash University [16]. The data were filtered to remove the histories for Rayleigh scatters and interactions that occurred in the collimator or housing as no *a-priori* knowledge of this information can be recorded experimentally. A total of 5.0×10^8 events were generated from the triple-intensity phantom. To provide realistic measurement data, uncertainties due to the nominal spatial and energy resolutions of the experimental detectors were added to the ideal data. The Compton interaction sequences were then randomized and re-ordered using a version of Bayesian reconstruction [17] where the source location was assumed to be at negative infinity on the *x*-axis.

Fig. 6(a) shows the statistics for Compton events as a function of event fold (the number of interactions in an event) for the square and cylindrical geometries. The cylindrical collimator yielded increases of 14.9% and 19.0% in the numbers of total and successfully ordered events, respectively, in comparison with the square collimator. An increase was achieved even though the open-fraction of the square collimator is greater. The percentage of successfully tracked events for the cylindrical geometry was 66.0%, compared to 63.7% for the square geometry. Although these rates were less than perfect, the majority of the unsuccessfully ordered events were not included in the image estimate as they were attenuated in transmission correction. Improved ordering could be achieved by incorporating the collimator geometry into the ordering algorithm, however it would be extremely computationally

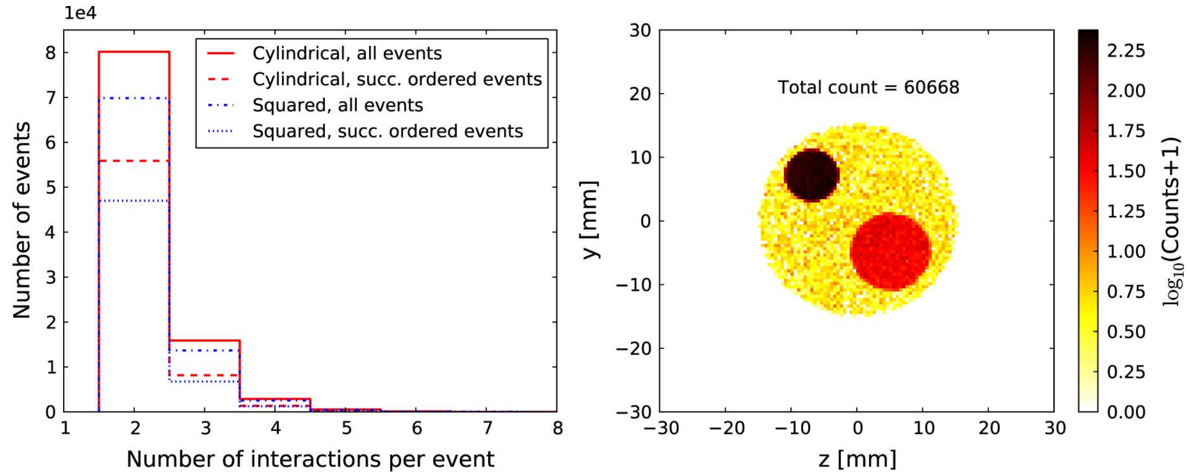

(a) (b)

Fig. 6. (a) A plot showing the number of events as a function of the number of interactions in the event for the two collimator configurations. (b) A 2D histogram in log-scale showing the photon emission positions, at the source plane, for events that passed through the cylindrical collimator and interacted in the detector-stack.

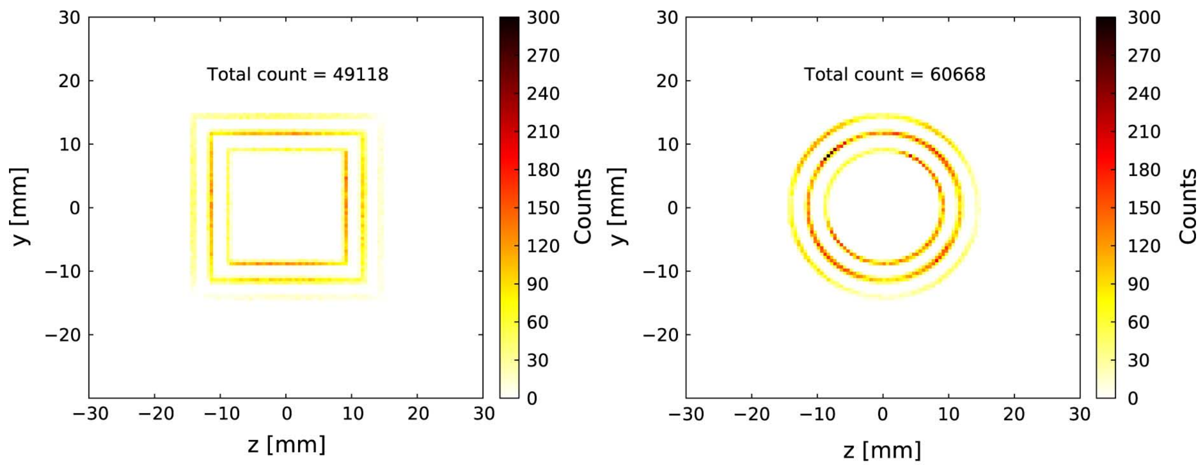

(a) (b)

Fig. 7. 2D histograms of the positions at which the photon emission vectors intersect the collimator plane for all detected Compton scattered events for (a) the square and (b) the cylindrical geometries, respectively. The complex variation in intensity shown between (a) and (b) is due to the combination of the change in the number of emitted photons that intersect the different regions of the collimators as a function of distance from the center of the FoV and the asymmetric source distribution.

intensive to test every permutation and so this extension was not included. For the result shown in Fig. 6(a), the realistic resolved/unresolved ratios are 0.143 and 0.161 for squared- and cylindrical collimators, respectively. From a comparable simulation, where the outer region of the collimator was completely open, the mean resolved/unresolved ratio was calculated to be 0.190. The lower resolved/unresolved ratios can be attributed to multiple scatter events being clustered into single pixels and the inclusion of housing interactions in the collimator data set but not in the comparable simulation one. Fig. 6(b) shows the 2D event histogram of the photon emission positions, at the source plane, for events that passed through the cylindrical collimator and interacted in the detector-stack. The distribution closely resembles the phantom shown in Fig. 5, and shows that the FoV of the slits covers the entire distributed planar phantom. The equivalent distribution for the events that passed through the square-slit collimator is very similar and is therefore not shown.

Fig. 7(a) and (b) show 2D histograms of the positions at which the photon emission vectors intersect the collimator plane for all detected Compton scattered events for the square and cylindrical geometries, respectively. The narrow distributions closely reproduce the precise outlines of the collimator apertures. This agreement demonstrates the effectiveness of the design at minimizing the number of unresolved events—events for which the primary scatter occurs in the collimator—that compose the data set. The variation in intensity shown in Fig. 7(a) and (b) is due to the combination of several geometrically varying parameters. These parameters include the source emission in spherical coordinates, the "Cartesian nature" of the detector stack and the asymmetric source distribution. In addition, for the cylindrical slit geometry, the intensity of the histogram is maximum in the regions of corners of the squared detectors where there is greater intersection of the rays with the detector stack. From these distributions, the cylindrical collimator has been shown to outperform the square collimator.

B. Reconstruction Results

The event data described in Section IV-A were reconstructed utilizing the technique described in Section III-C. The intersection of each back-projected CoR with each voxel in the imaging volume was calculated and summed. In order to reduce the computation time, p_{v1}, p_{12} and p_i were set to 1.0. Although these terms will ultimately effect the final image, their contribution is small compared to the other parameters that describe the $p_\wedge(\theta_v \mid \theta_C)$. Also, they will have a similar effect on both the ideal (excluding energy and spatial uncertainties) and realistic (including energy and spatial uncertainties) images reconstructed for each test case. Therefore setting these three parameters to unity was deemed to have a minimal effect on the study of the collimator performance. For each case, both the ideal and realistic image estimates were reconstructed to investigate the subsequent change in performance. The effects of the collimator on the image reconstruction were also investigated by performing back-projections with and without the collimator transmission function. It should be noted that while the GEANT4 data was blurred with the expected levels of experimental position and energy resolutions and Bayesian interaction ordering, no attempt has yet been made to estimate the performance of the code with time uncertainty that would result in pile-up and random coincidence.

Fig. 8(a) and (b) show the image estimates, at the depth where the source was located ($x = -60$ mm), for data collected with the square collimator and without inclusion of the collimator transmission function (i.e., cone-surface back-projection). The back-projection results from ideal data are shown on the left, while those using realistic experimental factors are shown on the right. The source appears as a single unresolved distribution in both cases and the size of this distribution is shown to increase significantly with the application of the experimental factors. Under these conditions, the data from the cylindrical collimator also resulted in similar distributions and so is not presented.

Fig. 8(c) and (d) show image estimates from the same data as is presented in Fig. 8(a) and (b), however, the collimator transmission function has also been included in each back-projection. The resulting reconstructions have a significant reduction in the level of overall blur and the high intensity source distribution is now visible above the background. However, there are still significant artifacts in the horizontal and vertical directions, caused by preferential modulation of the back-projected CoRs. Fig. 8(e) and (f) show equivalent representations to those in Fig. 8(c) and (d), however the simulated data were generated with a cylindrical shaped collimator. The resulting back-projections for this configuration enable isotropic modulation of the CoRs which results in a substantial reduction in image artifacts. The high intensity profile can easily be differentiated from the other features and the intermediate intensity distribution can also be observed. Additionally, There is a reduction of about 2 times in image intensity from ideal back-projection (left) to realistic back-projection (right) in Fig. 8. This is because of the effect of the additional spatial and energy uncertainties on blurring of the back-projected PDF of each CoR and decreasing the success rate of the Bayesian tracking algorithm. The noise in the images shows that the image quality can be improved with more event data.

In order to quantify the quality of different image estimates the contrast and noise properties for the three features and the background were measured by overlaying the exact phantom. The labelled regions I1, I2, I3 and B on the phantom shown in Fig. 5 are used as the template for the calculations, i.e., those regions are masked off when calculating the various contributions to contrast and SNR. As an example of the calculation, the contrast between regions I3 and I1 was obtained by dividing the difference of the mean intensities of regions I3 and I1 by the sum of the mean intensities, or $\langle I3\rangle - \langle I1\rangle / \langle I3\rangle + \langle I1\rangle$. Table II shows the contrast for each of the regions of the images reconstructed from data collected using the square collimator, with and without the inclusion of the collimator transmission function, and the cylindrical collimator with the inclusion of the transmission correction. In the table, *B* denotes the mean background level. For both the ideal and realistic data, the contrast between the intermediate intensity circle (*I2*) and the low intensity circle (*I1*) is completely dominated by the criss-cross artifacts. However, the contrast of *I3:I1*, *I2:I1* and *I1:B* increase significantly with the inclusion of the transmission function. When the cylindrical collimator is used, the contrast further increases in all cases for both the ideal and realistic data.

Table III shows the signal-to-noise-ratio (SNR). The SNR was calculated as $\langle I_N\rangle / \langle B\rangle$ for each distribution. In this instance the "signal" refers to mean intensities of the image regions where an emission was produced, when overlaying the exact phantom. Whereas the "noise" refers to the mean intensity of the image region from where no emissions were generated. For both collimator geometries, the SNR increases significantly with the inclusion of the transmission correction. The improvement in the SNR for the square collimator with the transmission function was 126%, on average. By moving from the square geometry to a cylindrical geometry, a further average increase of 31% was obtained. Repeat data sets were produced and the SNR values of calculated. The variations in SNR between the data sets was shown to be less than 10%.

V. System Point-Spread-Function (PSF)

A single point source was positioned in the center of the FoV in order to assess the affect of including large-area-apertures on the resolution of the system. Two configurations were considered, the Compton camera stack both with and without the cylindrical collimator. GEANT4 simulations were performed for which 1.0×10^7 event histories were generated. The total number of detected events were 1.57×10^6 and 4.7×10^4, respectively. This means that the slit openings on the collimator enabled 3.0% of all possible events to be detected, however it should be remembered that the central region of the collimator was reserved for pinholes. If this central region were allocated further large-area-slits, this fraction would be much greater. In fact the number of events that would pass through the three central pinholes is only 2.3% of the data that passes through the slits in the outer regions.

Fig. 9(a) and (c) show the image estimate and slice at $y = 0.0$ for the system without a mechanical collimator. As with all the data presented in this work, all detected events were included and there was no minimum threshold applied to the acceptance angle or distance between scatters. The FWHM of the PSF was estimated to be at least 42.0 mm. Clearly, no modulation can be applied to the back-projected CoRs. Fig. 9(b) and (d) shown the image estimate and slice at $y = 0.0$ for the system with

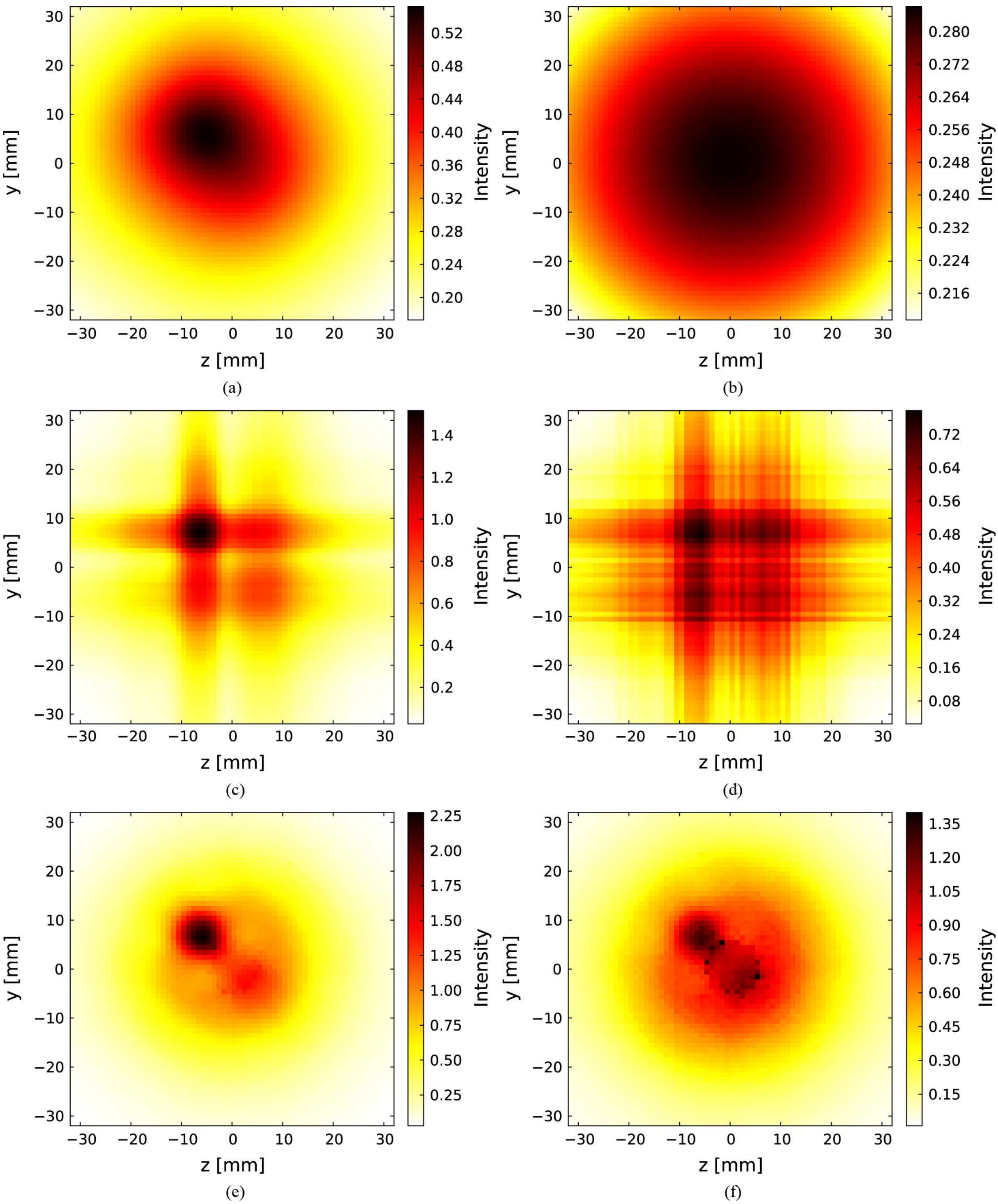

Fig. 8. Image estimates at the volume slice where the source was located. (a)-(d) were generated with data from the square collimator and (e)-(f) with data from the cylindrical collimator. The left column shows image estimates reconstructed from ideal data. The right column shows image estimates from data with experimental factors applied. (c) and (d) show the improvement achieved with the inclusion of the transmission function, with respect to (a) and (b). (e) and (f) show the further gains achieved through moving from a square to cylindrical geometry.

the cylindrical collimator. The modulation transmission function was applied to each CoR in back-projection. The FWHM of the realistic PSF in Fig. 9(d) is shown to be reduced to 2.0 mm, or by a factor of 20 with respect to the bare Compton camera. However, tails resulting from asymmetric modulation across the three concentric large-area-slits results in a broadening at the base of the distribution.

VI. Conclusion

The design of a hybrid collimator for the PEDRO prototype detector has been investigated. The aim was to find a realistic geometry that would enable optimized large-area slits to be included in the outer regions of a collimator to improve the sensitivity and increase the FoV. The constraints were to ensure that

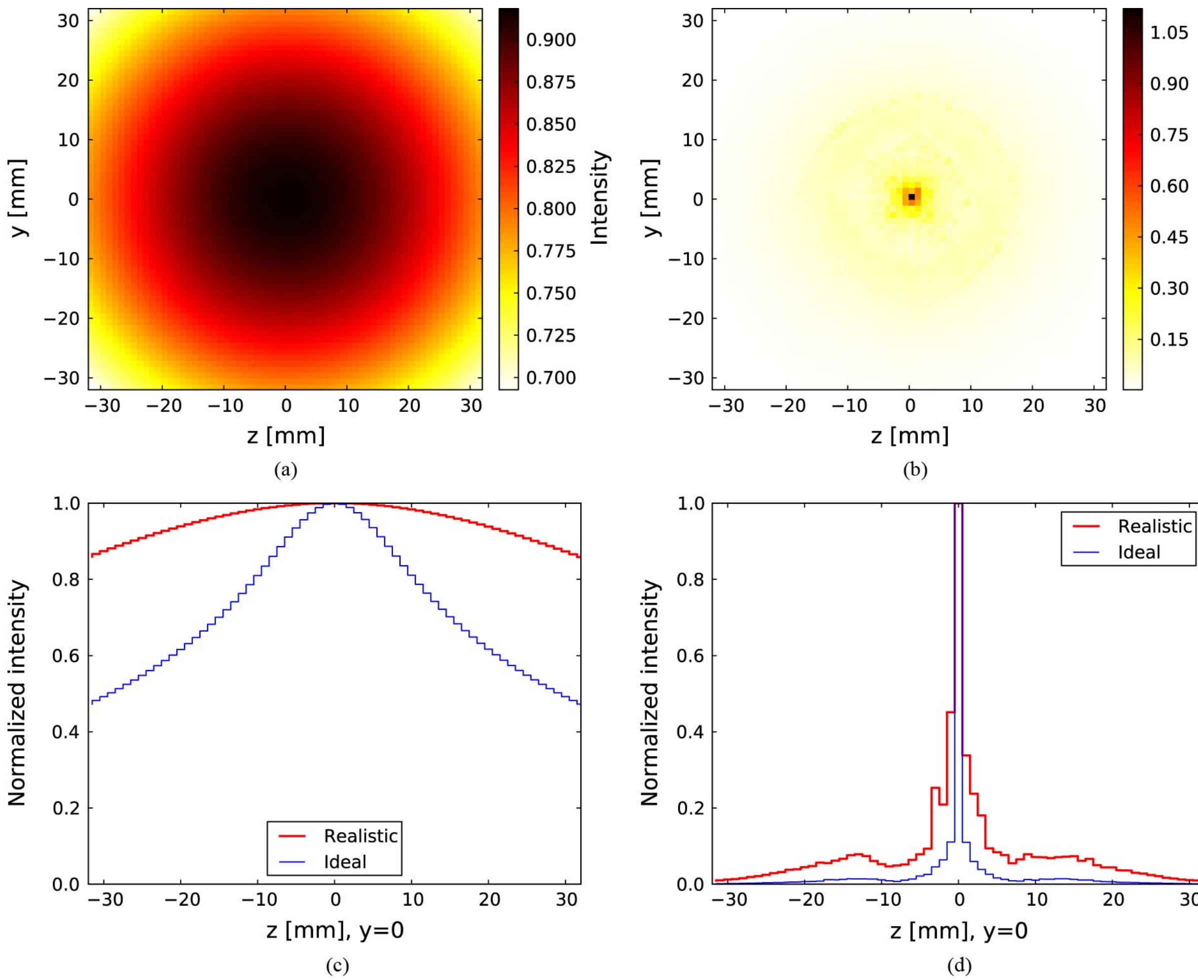

Fig. 9. Image estimates of the single point source obtained without any collimator (left) and with the cylindrical collimator (right). (a)-(b) are back-projection image estimates with realistic conditions. (c)-(d) are the distributions across the image estimates at y = 0, with both ideal and realistic conditions. With the cylindrical collimator, the FWHM of the realistic PSF in (d) is at least 20 times smaller than without the collimator.

TABLE II
IMAGE CONTRAST FOR THE SQUARE AND CYLINDRICAL COLLIMATORS.

		Square w/o trans.	Square w/ trans.	Cylindrical w/ trans.	Phantom
Ideal	I3:I1	0.098	0.297	0.334	0.916
	I2:I1	-0.009	0.024	0.099	0.818
	I1:B	0.238	0.500	0.571	1.000
Realistic	I3:I1	0.002	0.134	0.171	0.916
	I2:I1	0.004	0.021	0.093	0.818
	I1:B	0.055	0.401	0.515	1.000

TABLE III
SNR FOR THE SQUARE AND CYLINDRICAL COLLIMATORS.

		Square w/o trans.	Square w/ trans.	Cylindrical w/ trans.
Ideal	I3:B	1.975	5.546	7.342
	I2:B	1.595	3.149	4.467
	I1:B	1.623	3.003	3.664
Realistic	I3:B	1.122	3.001	4.412
	I2:B	1.125	2.439	3.769
	I1:B	1.117	2.340	2.126

the additional slits did not affect the image estimate that could be collected with the multi-pinhole configuration in the center of the aperture array.

It has been shown that the optimization technique developed allowed the large-area slits to not only fully sample the primary FoV, but also to extend this to enable region-of-interest analysis. The algorithm also enables the user to adjust the optimized slits to trade-off the FoV and sensitivity.

Square- and cylindrical-slit geometries were tested and the effect of accounting for the collimator transmission functions was also investigated. For both geometries, the results have shown that the collimator transmission function modulated the back-projected CoRs into the imaging volume and significantly improved the image quality quantified by contrast and SNR. It was also found that a cylindrical geometry collimator outperformed a square geometry collimator. The isotropic modulation of the cone surfaces resulted in less artefacts and more highly resolved image estimates. Also, the cylindrical geometry provided increased sampling of the FoV due to more optimal positioning of the slits. From data collected with the cylindrical collimator and a single point source in the center of the FoV, the resolution of the system was improved by a factor of 20, as compared to the uncollimated Compton camera. Although a resolution of ≥ 2.0 mm is not sufficient for small animal imaging, it is expected that this high statistics data will be utilized to compliment the high resolution pinhole data and improve the reconstruction. It is also likely that further gains are possible. Also, techniques where resolutions of the order of ≥ 2.0 mm can be obtained with relatively high statistics data sets are useful in other applications of SPEI.

Future work will involve both comparing and combining the pinhole data and large-area aperture Compton data in the framework of a maximum likelihood expectation maximization (ML-EM) reconstruction. A more realistic phantom for small animals, such as the Derenzo phantom, will be used to investigate the limits of image resolution and contrast that can be achieved for clusters of small features.

APPENDIX

Collimator Transmission Function: The slits on the collimator limit the cone back-projections as only certain gamma ray trajectories have a significant probability of traversing the Tungsten. The collimator transmission is given by,

$$p_t(\mathbf{r_{v1}}) = \exp\left[-\mu_W^t L_W(\mathbf{r_{v1}})\right] \tag{11}$$

where $L_W(\mathbf{r_{v1}})$ is the length that $\mathbf{r_{v1}}$ intersects with the collimator material. The collimator transmission function has values $0 \leq p_t(\mathbf{r_{v1}}) \leq 1$, depending on the thickness of Tungsten traversed. To obtain $L_W(\mathbf{r_{v1}})$, a 3D ray-tracing algorithm was implemented. Currently, to simplify the calculation, $p_t(\mathbf{r_{v1}})$ was set to zero for $\forall L_W(\mathbf{r_{v1}}) > 0$. The effect of the collimator transmission function is demonstrated in Fig. 4(a) and (b). The transmission function truncates the cone surface and therefore reduces the number of possible locations from which the source emission may have occurred. It was also found to improve the accuracy of the gamma-ray tracking algorithms as the majority of the false interaction orderings cannot be traced back through the collimator.

Detector Interaction Probabilities: The probability that a Compton scatter occurs in a detector is given by [18],

$$p_C = \frac{\mu_{Si}^C(e_0, Z)}{\mu_{Si}^t(e_0, Z)} \exp\left[-\mu_{Si}^t L_{Si}(\mathbf{r_{v1}})\right] \tag{12}$$

where $\mu_{Si}^C(e_0, Z)$ is the incoherent scattering linear attenuation coefficient and $\mu_{Si}^t(e_0, Z)$ is the total attenuation coefficient. For a stack geometry such as PEDRO, the probability that the photon traversed all other detectors between the source and $\mathbf{r_1}$ can also be included. This probability is given by,

$$p_{v1} = \exp\left[-\mu_{Si}^t L_{Si}(\mathbf{r_{v1}})\right]. \tag{13}$$

Following the initial scatter, the photon must then escape the primary interaction detector and traverse all other material intersected along $\mathbf{r_{12}}$. This probability is given by,

$$p_{12} = \exp\left[-\mu_{Si}^t L_{Si}(\mathbf{r_{12}})\right]. \tag{14}$$

Finally the photon must undergo a second interaction at $\mathbf{r_2}$, with probability,

$$p_i = 1 - \exp\left[-\mu_{Si,HPD}^t L_{Si,HPD}^{hit}(\mathbf{r_{12}})\right] \tag{15}$$

where $\mu_{Si,HPD}^t$ and $L_{Si,HPD}^{hit}$ are the linear attenuation and depth of intersection of the detector, either Si or HPD, at the second interaction.

Scattering Distribution Function: Given a Compton scatter is recorded, the angular probability for unpolarized incident photons is governed by $p(\theta_C)$, the scattering corrected Klein-Nishina cross section [19], [20], given by,

$$p(\theta_C) = K \frac{d\sigma_{KN}}{d\Omega}\Big|_{\theta_C} \cdot \sin\theta_C \cdot S(x, Z) \tag{16}$$

where K is a normalization factor so that $\int_0^\pi p(\theta)d\theta = 1$, $S(x, Z)$ is incoherent scattering function with $x = \sin\theta/\lambda(\dot{A})$ and $\lambda(\dot{A}) = 12.39852/e_0(keV)$. $S(x, Z)$ is material dependent and its functional dependence can be found in [21], $d\sigma_{KN}/d\Omega|_{\theta_C}$ is Klein-Nishina cross section at θ_C given by,

$$\frac{d\sigma_{KN}}{d\Omega}\Big|_{\theta_C} = \frac{r_e^2}{2}\left(\frac{e_1}{e_0}\right)^2\left(\frac{e_0}{e_1} + \frac{e_1}{e_0} - \sin^2\theta_C\right) \tag{17}$$

where $r_e = e^2/(4\pi\epsilon_0 m_e c^2) = 2.818 \times 10^{-15}\mathrm{m}$ is the classical electron radius.

Angular Uncertainty Function: For an arbitrary gamma ray, $\mathbf{r_{01}}$ has a magnitude r_{01}. Similarly, the first and second interaction positions $\mathbf{r}_1$ and $\mathbf{r_2}$ define a vector $\mathbf{r_{12}}$ with magnitude r_{12}. The angular uncertainty due to detector spatial resolution is described in [22] as,

$$\Delta\theta_r = \frac{\Delta r_1}{r_{v1}}\sqrt{1 + \alpha^2(1 + \beta^2) + 2\alpha\cos\theta_C} \tag{18}$$

where $\alpha = r_{v1}/r_{12}$, $\beta = \Delta r_2/\Delta r_1$, Δr_1 and Δr_2 are the spatial resolutions of the detectors in which the first and second interactions occurred (see Table I).

The angular uncertainty due to energy resolution can be obtained from the derivative of (7) with respect to the energy of the scattered photon e_1 [23]. The uncertainty is expressed as,

$$\Delta\theta_E = \frac{m_e c^2}{e_1^2 \sin\theta_C}\Delta E_T \tag{19}$$

where ΔE_T is the total energy uncertainty caused by Doppler Broadening (ΔE_D) and detector energy resolution (ΔE_R). The energy uncertainty due to Doppler Broadening can be approximated according to [24], [25] ,

$$\Delta E_D \approx \frac{e_1}{e_0}\sqrt{e_0^2 + e_1^2 - 2e_0 e_1\cos\theta_C}\frac{\Delta p_z}{m_e c} \tag{20}$$

where $\Delta p_z/m_e c$ is the dimensionless FWHM of the Compton profile. From [26] and [24], $\Delta p_z/m_e c$ for Si and CdTe are equal to 0.95×10^{-2} and 2.03×10^{-2}, respectively.

Combined with the FWHM of the detector energy resolution ΔE_R, the total energy uncertainty becomes,

$$\Delta E_T = \sqrt{\Delta E_R^2 + \Delta E_D^2} \tag{21}$$

and the total angular uncertainty is:

$$\Delta\theta = \sqrt{\Delta\theta_r^2 + \Delta\theta_E^2}. \tag{22}$$

ACKNOWLEDGMENT

The authors wish to acknowledge Monash University for the use of their Nimrod software in this work.

REFERENCES

[1] S. Metzler, R. Accorsi, A. Ayan, and R. Jaszczak, "Slit-slat and multi-slit-slat collimator design and experimentally acquired phantom images from a rotating prototype," *IEEE Trans. Nucl. Sci.*, vol. 57, pp. 125–134, 2010.

[2] S. Meikle, P. Kench, A. Weisenberger, R. Wojcik, M. Smith, S. Majewski, S. Eberl, R. Fulton, A. Rosenfeld, and M. Fulham, "A prototype coded aperture detector for small animal SPECT," in *Nuclear Science Symp. Conf. Record*, 2002, vol. 3, pp. 1580–1584.

[3] J. Qian, E. Bradley, S. Majewski, V. Popov, M. Saha, M. Smith, A. Weisenberger, and R. Welsh, "A small-animal imaging system capable of multipinhole circular/helical SPECT and parallel-hole SPECT," *Nucl. Instrum. Methods Phys. Res. A*, vol. 594, pp. 102–110, 2008.

[4] S. Motomura, S. Enomoto, H. Haba, K. Igarashi, Y. Gono, and Y. Yano, "Gamma-ray Compton imaging of multitracer in biological samples using strip germanium telescope," *IEEE Trans. Nucl. Sci.*, vol. 54, pp. 710–717, 2007.

[5] M. Dimmock, J. Gillam, T. Beveridge, J. Brown, R. Lewis, and C. Hall, "A pixelated emission detector for radioisotopes (PEDRO)," *Nucl. Instrum. Methods Phys. Res. A*, vol. 612, pp. 133–137, 2009.

[6] N. Clinthorne, C. Ng, C. Hua, J. Gormley, J. Leblanc, S. Wilderman, and W. Rogers, "Theoretical performance comparison of a Compton-scatter aperture and parallel-hole collimator," in *Proc. Nuclear Science Symp.*, 1996, vol. 2, pp. 788–792.

[7] B. Smith, "Reconstruction methods and completeness conditions for two Compton data models," *J. Opt. Society Amer. A*, vol. 22, pp. 445–459, 2005.

[8] B. Smith and L. Denbina, "Cameras shapes for medical imaging Compton cameras," *Proc. SPIE*, vol. 7805, p. 780512, 2010.

[9] D. Wilson, H. Barrett, and E. Clarkson, "Reconstruction of two-and three-dimensional images from synthetic-collimator data medical imaging," *IEEE Trans. Med. Imaging*, vol. 19, pp. 412–422, 2002.

[10] S. Midgley, A. Berry, N. Benci, S. Morton, D. Phillips, P. Smith, S. Troja, and R. Lewis, "Hybrid pixel detector development for medical radiography," *Nucl. Instrum. Methods Phys. Res. A*, vol. 573, pp. 129–132, 2007.

[11] A. Lynch, A. Berry, G. Panjkovic, and R. Lewis, "Generic data acquisition system for multi-dimensional radiation detectors," in *IEEE Nuclear Science Symp. Conf. Record, NSS'07*, 2008, vol. 1, pp. 478–481.

[12] L. Meng, W. Rogers, N. Clinthorne, and J. Fessler, "Feasibility study of Compton scattering enhanced multiple pinhole imager for nuclear medicine nuclear science," *IEEE Trans. Nucl. Sci.*, vol. 50, pp. 1609–1617, 2003.

[13] S. Agostinelli, J. Allison, K. Amako, J. Apostolakis, H. Araujo, P. Arce, M. Asai, D. Axen, S. Banerjee, and G. Barrand, "Geant4-a simulation toolkit," *Nucl. Instrum. Methods Phys. Res. A*, vol. 506, pp. 250–303, 2003.

[14] S. Wilderman, J. Fessler, N. Clinthorne, J. LeBlanc, and W. Rogers, "Improved modeling of system response in list mode EM reconstruction of Compton scatter camera images," *IEEE Trans. Nucl. Sci.*, vol. 48, pp. 111–116, 2001.

[15] D. S. Vickers, "Collimator for Radiation Detectors and Method of Use," U.S. patent 7612343, 2009.

[16] D. Abramson, J. Giddy, and L. Kotler, "High performance parametric modeling with Nimrod/G: Killer application for the global grid?," in *Proc. Int. Parallel and Distributed Processing Symp. (IPDPS)*, Cancun, Mexico, May 2000, pp. 520–528.

[17] G. Pratx and C. Levin, "Bayesian reconstruction of photon interaction sequences for high-resolution PET detectors," *Phys. Med. Biol.*, vol. 54, pp. 5073–5094, 2009.

[18] S. Wilderman, N. Clinthorne, J. Fessler, C. Hua, and W. Rogers, "List mode EM reconstruction of Compton scatter camera images in 3-D," in *Proc. IEEE Nuclear Science Symp.*, vol. 3.

[19] D. Cullen, "A simple model of photon transport," *Nucl. Instrum. Methods Phys. Res. A*, vol. 101, pp. 499–510, 1995.

[20] T. Kragh, "Tradeoffs and Limitations in Statistically Based Image Reconstruction Problems," Ph.D. dissertation, The Univ. Michigan, Ann Arbor, 2002.

[21] J. Hubbell, W. Veigele, E. Briggs, R. Brown, D. Cromer, and R. Howerton, "Atomic form factors, incoherent scattering functions, and photon scattering cross sections," *J. Phys. Chem. Ref. Data*, vol. 4, pp. 471–538, 1975.

[22] C. Ordonez, W. Chang, and A. Bolozdynya, "Angular uncertainties due to geometry and spatial resolution in Compton cameras," *IEEE Trans. Nucl. Sci.*, vol. 46, pp. 1142–1147, 1999.

[23] A. Zoglauer and G. Kanbach, "Doppler broadening as a lower limit to the angular resolution of next-generation Compton telescopes," in *Proc. Society of Photo-Optical Instrumentation Engineers (SPIE) Conf. Series*, 2003, vol. 4851, pp. 1302–1309.

[24] G. Matscheko, G. Carlsson, and R. Ribberfors, "Compton spectroscopy in the diagnostic x-ray energy range: II. Effects of scattering material and energy resolution," *Phys. Med. Biol.*, vol. 34, pp. 199–208, 1989.

[25] M. Hirasawa and T. Tomitani, "An analytical image reconstruction algorithm to compensate for scattering angle broadening in Compton cameras," *Phys. Med. Biol.*, vol. 48, pp. 1009–1026, 2003.

[26] F. Biggs, L. Mendelsohn, and J. Mann, "Hartree-Fock Compton profiles for the elements," *Atomic Data Nucl. Data Tables*, vol. 16, pp. 201–309, 1975.